

The Sensitivity of Microwave Remote Sensing Observations of Precipitation to Ice Particle Size Distributions

RALF BENNARTZ*

Institut für Weltraumwissenschaften, Freie Universität Berlin, Berlin, Germany

GRANT W. PETTY⁺

Department of Earth and Atmospheric Sciences, Purdue University, West Lafayette, Indiana

(Manuscript received 22 April 1999, in final form 17 February 2000)

ABSTRACT

This study investigates the effect of variable size distribution and density of precipitation ice particles on microwave brightness temperatures. For this purpose, a set of self-consistent relationships among rain rate, size parameters of an exponential drop size distribution, and the radar reflectivity–rain rate relations for frozen and liquid precipitation was derived. Further, a scaling factor was introduced that is the ratio between the average melted diameter of the frozen and liquid precipitation and allows the specification of different sizes of the frozen particles. For given radar observations, this method allows size distributions of frozen and liquid precipitation to be derived, which are then used as input for a radiative transfer model.

These relationships were used to perform Mie calculations for different precipitation rates and different types of hydrometeors (snow, graupel, and hail) and to investigate the dependence of their respective optical properties on rain rate as well as on the radar reflectivity. It is shown that, for a given rain rate, variations of particle density as well as of particle size may result in variations of the extinction coefficient by an order of magnitude. However, a comparison of volume extinction coefficients with radar reflectivities found that, for a broad range of particle sizes, the particle density has little effect in comparison with the liquid-equivalent size of the ice particles.

The proposed method was applied to cases of coincident Special Sensor Microwave Imager (SSM/I) and radar volume scans, the latter being provided by the Swedish Gotland radar. Microwave optical fields for all four SSM/I frequencies were derived from the radar data, and the observed brightness temperature was simulated using a three-dimensional Monte Carlo radiative transfer model. A comparison of scattering indices at 85 GHz derived from the SSM/I overpass with those derived from the model data found that the size of the precipitation-sized ice particles governs the variability of the scattering index. For the particular cases investigated here, the ice particle size varied considerably depending on the type of the precipitation event. For the case of an intensive thunderstorm, ice particles are roughly four times larger than liquid precipitation at the same rain rate, but the ice particles of a frontal system are inferred to be only 20% larger than liquid ice particles. A further evaluation of the relation between scattering index and radar-derived precipitation intensity above the freezing level found high correlations (0.8–0.9) for all precipitation events. However, the sensitivity of scattering index to precipitation intensity varies within a broad range for different types of precipitation events. A convective event had a sensitivity of $9 \text{ K (mm h}^{-1}\text{)}^{-1}$, but frontal and small-scale convective events showed sensitivities in the range between 20 and $50 \text{ K (mm h}^{-1}\text{)}^{-1}$.

1. Introduction

Several microwave retrieval algorithms for precipitation rely entirely on the scattering signature of precipitation-sized ice particles (e.g., Grody 1991; Adler

et al. 1993). The advantage of using this scattering information is that 1) sensitivity is similar at both light and heavy precipitation rates and 2) it is capable of providing information about precipitation over strongly emitting surfaces and hence is the primary basis for estimating precipitation rate over land. However, the correlation of scattering intensity and instantaneous rain rate at the surface has been found to be weak, reflecting the broad variety of cloud microphysical processes involved in the precipitation formation for different types of precipitation. Recent studies of midlatitude frontal and convective systems indeed indicate that the relation between scattering indices and precipitation intensity

* Current affiliation: Department of Physics and Astronomy, University of Kansas, Lawrence, Kansas.

⁺ Current affiliation: Department of Atmospheric and Oceanic Sciences, University of Wisconsin—Madison, Madison, Wisconsin.

Corresponding author address: Ralf Bennartz, Department of Physics and Astronomy, University of Kansas, Lawrence, KS 66045.
E-mail: bennartz@ukans.edu

might systematically vary with the type of precipitation (Todd and Bailey 1995; Kidd 1998).

In the current study, we employ coincident precipitation radar and Special Sensor Microwave Imager (SSM/I) data to investigate this issue further. The hypothesis investigated here is that variations of the size of the ice particles can be responsible for variations of the ice-scattering signature observed for given rain rates. In section 2, we derive self-consistent relations between the drop size distribution of liquid precipitation and the corresponding size distribution of ice particles. We introduce a size ratio x , which describes the ratio between the average liquid equivalent diameter of the frozen hydrometeor and the diameter of the liquid precipitation. We further derive radar reflectivity–rainfall rate (Z – R) relations for frozen and liquid precipitation that are consistent with their respective size distributions and precipitation rate, which, in turn, depend on the drop size–dependent fall speed of the liquid/frozen precipitation. This method provides the basis for deriving hydrometeor profiles from the radar data and is described in section 2. Based on Mie calculations for different size factors, precipitation rates, and particle densities, we investigate the relative effect of these parameters on microwave optical properties (section 3).

In section 4 we apply the new method to three different precipitation events and evaluate the relative effect of ice particle size and density. The precipitation events were observed during the Baltic Sea Experiment–Pilot Study for Intensive Data Collection and Analysis of Precipitation (BALTEX–PIDCAP) during August and September 1995. We use three-dimensional radar data to derive particle size distributions and microwave optical properties. To minimize possible errors from beam filling and other three-dimensional effects, we employ a three-dimensional radiative transfer model and convolve the model results to the actual SSM/I observation geometries and footprint resolutions, thus simulating the complete SSM/I overpass. We apply the retrieval algorithms of Petty (1994b) to both the observed and simulated SSM/I data and compare brightness temperatures as well as derived scattering indices, the results of which are shown in section 4. Last, we compare radar precipitation estimates derived using the new method with the satellite-derived scattering index.

2. Theoretical considerations

a. Particle size distribution

Because the non-Doppler radar data provide only an effective reflectivity factor Z for a given grid cell, assumptions about the phase of the precipitation as well as of the particle size distribution have to be made in order to provide sufficient information for the passive microwave radiative transfer calculations as well as for Z – R conversion. Because a wide variety of hydrometeor size distributions, particle fall speeds, and Z – R relations

have been published, we take some effort to derive relations that are internally consistent yet flexible. The objective is to derive a precipitation intensity from the radar measurements, which, in turn, yields a size distribution from which we then can reproduce the same radar reflectivity again. Further, we introduce a size ratio x between the averaged radius of the frozen and the liquid precipitation, allowing us to adjust empirically the poorly known size distribution of the ice above the freezing level relative to the somewhat better-known size distribution of the liquid precipitation.

We define relations to convert size distribution parameters from liquid to frozen precipitation, fulfilling the requirement that, for a given rain rate, the average particle diameter of the frozen precipitation must differ by the factor x from that of the liquid precipitation. Note that, throughout this paper, we use the liquid equivalent diameter to characterize ice particle sizes, and note that all relationships assume an internal consistent set of physical units, such as the Système International d'Unités (SI). Introducing an exponential size distribution $N(D)$ and a particle terminal velocity $U(D)$, with N_0 and λ being functions of rain rate R and D being the melted diameter,

$$N(D) = N_0 e^{-\lambda D}, \quad (1)$$

$$N_0 = AR^b, \quad (2)$$

$$\lambda = CR^E, \quad \text{and} \quad (3)$$

$$U(D) = \alpha D^\gamma. \quad (4)$$

We obtain the following relations for the average diameter:

$$\frac{\int N_L(D) D \, dD}{\int N_L(D) \, dD} = x \frac{\int N_F(D) D \, dD}{\int N_F(D) \, dD}, \quad (5)$$

and for the precipitation rate:

$$\frac{\pi}{6} \int N_L(D) U_L(D) D^3 \, dD = \frac{\pi}{6} \int N_F(D) U_F(D) D^3 \, dD, \quad (6)$$

where all integral limits are zero to infinity, and the subscripts L and F refer to liquid and frozen precipitation, where frozen precipitation can be snow, graupel, or hail. Equation (6) enforces continuity of the precipitation rate across the melting level; Eq. (5) severely constrains the shape of the size distribution and thus might be understood as an idealization that facilitates the assessment of the particle size distributions. It is, however, a relaxation of the frequently used assumption that there is a one-to-one correspondence between ice particles and liquid particles; that is, each ice particle is melted to a single liquid particle (e.g., Bauer et al.

1999). In our model, this outcome would be the case if x is equal to 1.

Noting that the general solution of an integral of the form appearing in Eqs. (5) or (6) is

$$\int D^a e^{-\lambda D} dD = \frac{\Gamma(a+1)}{\lambda^{a+1}}, \quad (7)$$

we obtain from Eq. (5):

$$\lambda_F = x\lambda_L. \quad (8)$$

This result is independent of the exponent of D in Eq. (5), because $1/\lambda$ is the average diameter of the distribution. From Eq. (6), we can now derive an expression for N_{0F} . Because the terminal velocity of snow is much smaller than that of rain, an identical precipitation rate has to be maintained via an increase in particle concentration for the snow. Substituting Eqs. (1) and (2) into Eq. (6), we obtain

$$\frac{N_{0L}\alpha_L\Gamma(4+\gamma_L)}{\lambda_L^{(4+\gamma_L)}} = \frac{N_{0F}\alpha_F\Gamma(4+\gamma_F)}{\lambda_F^{(4+\gamma_F)}} \quad \text{and} \quad (9)$$

$$N_{0F} = N_{0L} \frac{\alpha_L\Gamma(4+\gamma_L)\lambda_F^{(4+\gamma_F)}}{\alpha_F\Gamma(4+\gamma_F)\lambda_L^{(4+\gamma_L)}}. \quad (10)$$

Equations (8) and (10) describe a transformation between the size distributions of frozen and liquid precipitation, given the ratio x of the melted diameters of the liquid to frozen precipitation. We now derive analytical expressions for the Z – R relationships for liquid and frozen precipitation that are solely based on the constants outlined in Eqs. (2)–(4) and for snow that are based on the size ratio x . The effective radar reflectivity for liquid precipitation can be derived from

$$Z_L = \int N_L(D)D^6 dD. \quad (11)$$

For frozen precipitation, the above equation requires an additional factor that accounts for the different dielectric constants of water and ice. Solving Eq. (11), we obtain

$$Z_L = N_{0L} \frac{\Gamma(7)}{\lambda^7}, \quad (12)$$

and plugging in Eqs. (1) and (2) yields a Z – R relation,

$$Z_L = \frac{A\Gamma(7)}{C^7} R^{(B-7E)}. \quad (13)$$

The same approach for snow gives

$$Z_F = \frac{0.197}{0.93} \Gamma(7) \frac{\alpha_L\Gamma(4+\gamma_L)}{\alpha_F\Gamma(4+\gamma_F)} A C^{(\gamma_F-\gamma_L-7)} x^{(\gamma_F-7)} \times R^{[B+(\gamma_F-\gamma_L-7)E]}, \quad (14)$$

where we used Eqs. (8) and (10) to replace λ_F and N_{0F} , and 0.197/0.93 is the ratio of the relevant dielectric property of water and ice. Last, we determine values

for the constants in Eqs. (2)–(4) such that self consistency is maintained between rain rates, Z – R relationship, the precipitation estimates derived from Eq. (6), and the reflectivity estimates from Eq. (11). For a given R , we may write

$$\begin{aligned} R &= \frac{\pi}{6} \int N_L(D)U_L(D)D^3 dD \\ &= \frac{\pi}{6} \int AR^B e^{-CR^E D} \alpha_L D^{\gamma_L} D^3 dD. \end{aligned} \quad (15)$$

Solving this integral yields

$$R^{[1-B+E(4+\gamma_L)]} = \frac{\pi}{6} A \alpha_L \frac{\Gamma(4+\gamma_L)}{C^{(4+\gamma_L)}}, \quad (16)$$

which must be valid for all rain rates. Therefore, setting R equal to 1, we obtain a relation between the parameter A and the remaining parameters,

$$A = \frac{6}{\pi \alpha_L \Gamma(4+\gamma_L)} C^{(4+\gamma_L)}. \quad (17)$$

Replacing A in Eq. (2) by this expression yields a value for B of

$$B = E(4+\gamma_L) + 1. \quad (18)$$

b. Radar beam model

Because the radar beamwidth and altitude strongly depend on distance, significant deviations of the radar reflectivities obtained at close and far distances from the radar may occur. Given a radar beamwidth of 0.9° and beam elevation of the radar scan of 0.5° , which are the actual values used for the Gotland radar scans, at distances from the radar of 200 km, the lowest radar beam has an elevation of 5.9 km (assuming standard refraction) and a beamwidth of roughly 3.2 km. The obvious conclusion is that at great distances there is little or no vertical information available in the radar data and all precipitation information is received from the topmost part of the frozen precipitation. This effect leads to the well-known dependence of radar rain estimates on distance. In order to apply a first-order correction for this effect, we shall introduce several assumptions about the vertical and horizontal structure of the precipitation and the radar beam itself.

- 1) The beam at a given distance from the radar is horizontally uniformly filled with precipitation; that is, beam-filling problems occur only in the vertical. This idealization is valid to high accuracy for widespread frontal precipitation; for horizontally inhomogeneous precipitation, such as convective showers, it is less appropriate.
- 2) We further assume that, in the vertical, the precipitation intensity is constant throughout the entire beam, regardless of the actual type of precipitation, which may vary with altitude. Note that this as-

sumption is only utilized at far ranges from radar, where only one piece of information is available for the entire column. At closer distances, the vertical variability of the precipitation intensity is obtained from the independent radar measurements at different altitudes.

- 3) In the vertical, the beam may consist of liquid precipitation, a melting layer, frozen precipitation, and entirely precipitation-free regions above cloud top. The liquid precipitation is assumed to be confined to the layer between the ground and the melting layer, which is 500-m thick and is bounded on the top by the freezing level. Frozen precipitation is assumed to exist from the freezing level up to the cloud top.
- 4) We do not explicitly consider physical processes that may affect the size distribution. This especially means that we treat the melting layer in a phenomenological way by simply stating that the backscattering intensity in the melting layer is a fixed amount larger than in the rain layer (we choose +4 dBZ).
- 5) The altitude of the top of the precipitation area z_{top} and freezing level z_{freez} must be specified. In practice, we derived the former from the radar data close to the radar site, where the vertical resolution is sufficient. It is then taken to be constant for the entire radar area. The latter is derived from the SSM/I estimate of the columnar water vapor path according to Petty (1994b).
- 6) The antenna pattern of the radar is assumed to be Gaussian, with 3-dB beamwidths as given by the specifications of the Swedish Meteorological and Hydrological Institute (SMHI), which operates the radar.

Now we can derive numerically the relative weights associated with each precipitation type by integrating the antenna pattern function over the altitude range that is covered by the precipitation type. Note that, because of assumption 1, the antenna pattern can be treated as one-dimensional. Given the above defined Z - R relations, we can calculate the radar reflectivity that would be observed for any given precipitation intensity. The precipitation rate that corresponds to the measured radar reflectivity is found by an iterative scheme, which usually converges within 5–10 steps. If the radar beam is assumed to be filled entirely with one type of precipitation, this scheme yields the same result as the standard Z - R relation. However, at far distances from the radar, where the relative weight of precipitation-free areas above cloud top increases, the scheme leads to a significant increase of precipitation intensity for a given radar reflectivity in comparison with the Z - R relation. Notwithstanding the correction scheme applied here, precipitation growth processes, such as collision-coalescence for raindrops or accretion of supercooled water by graupel, may strongly enhance the actual surface precipitation rate without having any measurable effect

on the estimated surface precipitation rate at far distances from the radar.

It is recognized that the above-outlined assumptions reflect a high degree of idealization, whose accuracy also depends on the type of precipitation itself. Most of these assumptions are assumed to be reasonable for frontal-type stratiform precipitation; for convective precipitation their accuracy might be quite limited. However, even if considerable horizontal variations occur within a given radar measurement, the sign of the correction, if not the magnitude, would be correct.

3. Comparison of optical properties derived for different types of hydrometeors

The passive microwave optical parameters can be calculated directly from Mie theory given the particle size distribution and density. For ice particles, we use the Maxwell-Garnett mixing rule to obtain the dielectric constants of the air-ice mixture. The above-described method (section 2) of deriving internally consistent microphysical parameters allows this information to be determined in a way such that the particle size distributions and densities are consistent with the observed radar data. In the next section, we discuss the effect of different types of variable ice particle size and of different hydrometeors (i.e., different densities of frozen particles) in terms of their microwave optical parameters.

a. Contribution of different drop sizes to the optical parameters

Figure 1 shows an example of the contribution of the different particle sizes to the total rain rate, radar reflectivity, and volume extinction for an exponential particle size distribution of snow at a precipitation intensity of 13 mm h^{-1} . The values are integrals over the respective spectral quantity over the interval $[0, D^*]$, where D^* is the abscissa value. Thus, the curves give the relative contribution of particles with diameter D less than D^* to the overall quantity. The different curves reflect different sizes of the ice particles as defined in Eq. (8). Although the integrated rain rate is independent of the size ratio x , the relative contribution of smaller drops to the total rain rate is larger for smaller ice particles. For the smallest particles at x equal to 3, only particles with D less than 2 mm significantly contribute to the total rain rate. For the largest particles shown here ($x = 0.3$), even particles larger than 8 mm would contribute to the total precipitation intensity. Such large particles are likely to break up during the melting process.

The integrated radar reflectivity and the volume extinction show significant variations that depend on the relative size of the ice particles. The volume extinction coefficient varies between roughly 4 km^{-1} for small ice particles and 11 km^{-1} for large ice particles. The radar

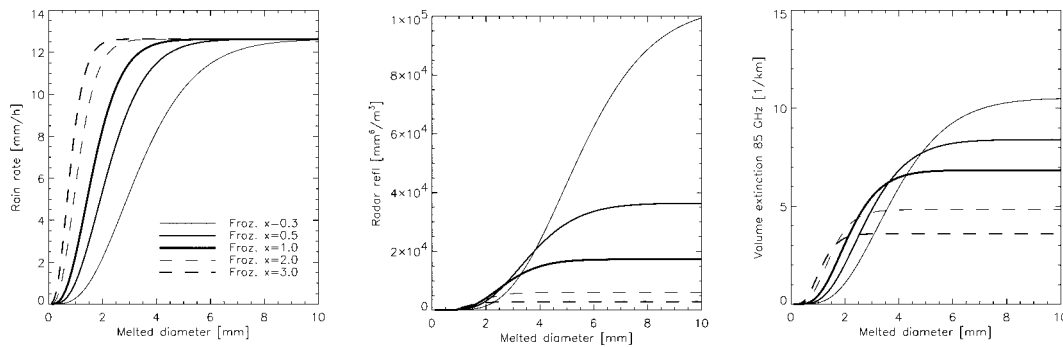


FIG. 1. Contribution of different sizes of hydrometeors to the total rain rate, radar reflectivity, and volume extinction coefficient for snow at 13 mm h^{-1} rain rate. Results are plotted for different values of the size ratio x , defined in Eq. (5), which is the ratio between the mean diameter of liquid precipitation with a given intensity and frozen precipitation of the same intensity. The abscissa gives the melted diameter (mm); the ordinate gives the integral from zero to this diameter of the respective variable.

reflectivity varies between $500 \text{ mm}^6 \text{ m}^{-3}$ (33 dBZ) and $10^5 \text{ mm}^6 \text{ m}^{-3}$ (50 dBZ). These results reflect the high degree of sensitivity of the microwave response to changes in the size distribution. Drops in the diameter range from 2 to 6 mm contribute most strongly to the radar reflectivity, whereas the smaller drops with diameter less than 4 mm largely control the volume extinction and rain rate.

b. Relation between optical properties and radar reflectivity

Applying the above outlined method, we compare the results of Mie calculations obtained for different types of frozen hydrometeors, namely, snow, graupel, and hail, which are henceforth assumed to be spherical particles with variable density and fall speed (Table 1). Except for raindrops, whose properties were chosen to yield exact consistency with the Marshall and Palmer (1948) drop size distribution, the values for fall speed and density of the different types of hydrometeors used in this study are adapted from Ferrier (1994) and the

references cited therein and are compiled in Table 1. Note that there are numerous different fall speed relations published for each of the hydrometeor types, and that fall speed relations also depend on the shape of ice crystals. The objective assessment of their respective accuracy and limitations is not possible within the framework of this paper. Our only selection criterion was to use well-established fall speed relations that satisfy Eq. (4). Only the constants C and E of Eq. (3) for liquid hydrometeors have to be given. All other constants are calculated from Eqs. (8)–(18). For example, for liquid water we may derive the constants A and B in Eq. (2) from Eqs. (17) and (18), yielding $B = 0$ and $A = 8000$ when R is given in millimeters per hour and N_0 is given per millimeter per cubic meter, or $A = 8.0 \times 10^6$ when expressed in SI units. By design, these values are exactly consistent with the constant value given for N_0 by Marshall and Palmer.

The most fundamental optical properties of a layer of the atmosphere that determine microwave radiances at a given wavelength are the volume extinction coefficient k_{ext} , the single-scatter albedo ω , and the asymmetry parameter g . The second of these quantities gives the ratio of scattering to total extinction (scattering plus absorption); the third is the average cosine of the scattering angle, with higher positive values indicating greater degrees of forward scattering.

Figure 2 shows the results of Mie calculations for 85 GHz, different precipitation intensities, and a number of different size ratios x of the frozen precipitation to liquid precipitation. For frozen precipitation, the extinction coefficient shows a power-law dependence on rain rate. The variability of the extinction coefficient induced by different sizes of the hydrometeors is less than one order of magnitude for a given precipitation intensity and hydrometeor type. In general, the smaller particles exhibit the smallest volume extinction coefficient. This result is despite the fact that, to sustain a given precipitation intensity, the particle concentration must increase to compensate for smaller fall speeds. The

TABLE 1. Density and fall speed parameters used in this investigation. Except for the parameters for rain, which were chosen for consistency with the drop size distribution of Marshall and Palmer (1948), this table reproduces the values given in Ferrier (1994), but converted to SI units (m, kg, s). The symbols α and γ refer to the parameters used in Eq. (4). The values C and E are used in Eq. (3) to derive the exponent λ of the distribution of liquid hydrometeors. It is important to note that all constants and relationships assume consistent use of SI units throughout. This assumption implies, for example, that rain rate R must be converted from millimeters per hour to meters per second before applying Eq. (3) and that the resulting λ has units of inverse meters.

	Density (kg m^{-3})	α	γ	C	E
Rain	1000.0	628.2	0.76	172.1	−0.21
Snow	100.0	8.97	0.42	—	—
Graupel	400.0	19.3	0.37	—	—
Hail	900.0	208.5	0.64	—	—

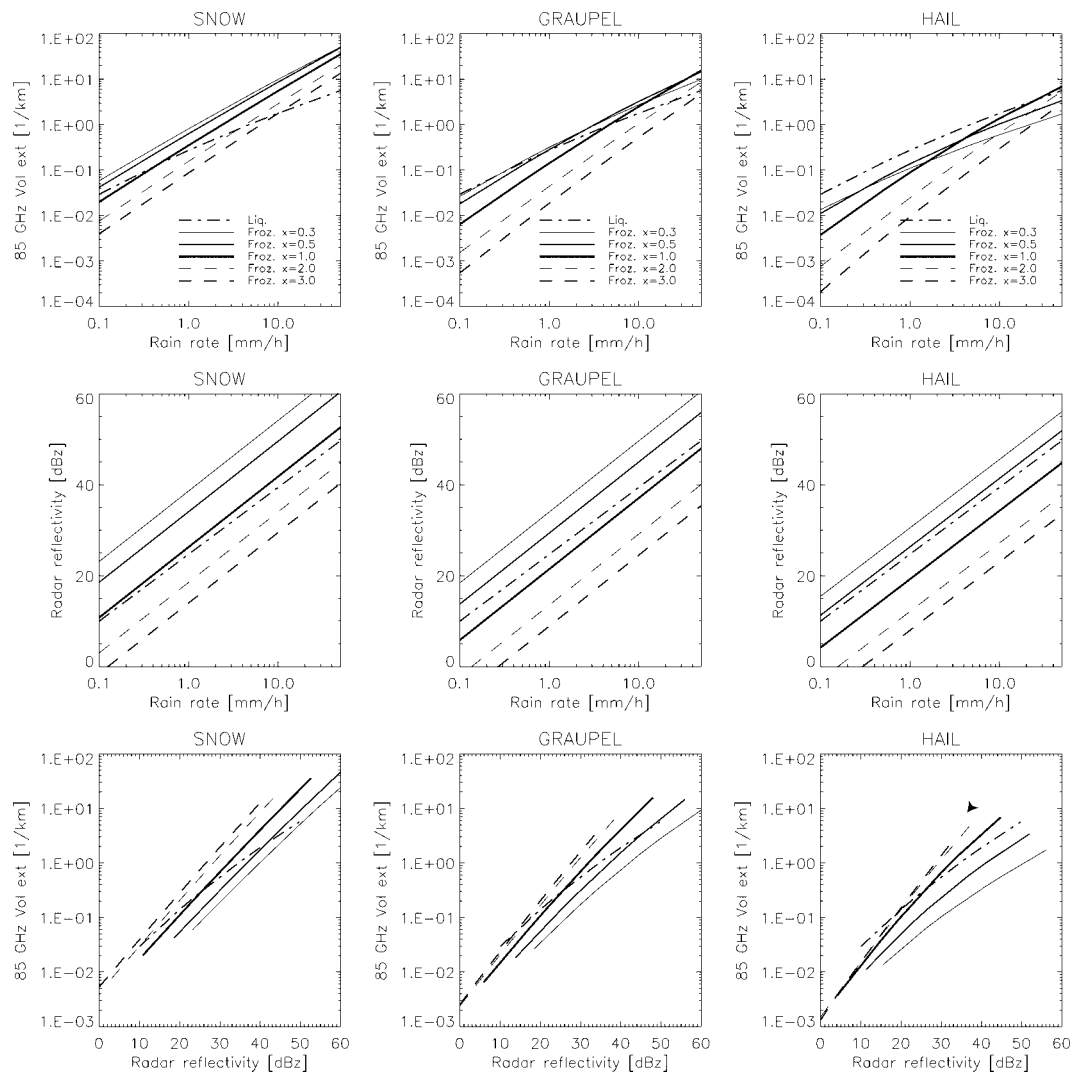


FIG. 2. The upper panels show the relation between precipitation intensity and 85-GHz extinction coefficient, the middle panels show the respective Z - R relation, and the lower panels show the relation between radar reflectivity and the 85-GHz extinction coefficient. Results for liquid precipitation are also shown. All calculations were performed for $T = 273.16$ K.

same variability as for the average diameter is seen for different types of hydrometeors. Extinction coefficients at 50 mm h^{-1} for snow are between 20 and 40 km^{-1} , depending on density; hail shows maximum values that are below 10 km^{-1} . For small rain rates, the derived quantities for hail are only of theoretical interest, because hail typically only occurs in strong convective events that produce heavy rainfall. Likewise, one may argue that precipitation intensities of dry snow are unlikely to reach 50 mm h^{-1} .

The Z - R relations derived for different size ratios x (see Fig. 2, middle panels) show largest values for the largest particles with $x = 0.3$. This result, however, is not surprising, given that the scattering intensity is proportional to the sixth power of the particle diameter. An interesting result of the comparison of the different Z - R

relations is that large particle diameters associated with low density show a radar reflectivity that is significantly higher than that of liquid precipitation. A frequent observation in frontal precipitation systems, however, is that above the melting layer the radar reflectivity is somewhat smaller than it is below the melting layer. This observation therefore constrains the maximum size of ice particles for frontal precipitation events. The size ratio x must be in a range such that the associated radar reflectivity falls below the radar reflectivity for liquid precipitation.

Comparing the 85-GHz extinction coefficients with the radar reflectivity (see Fig. 2, lower panels), one can see that for the frozen precipitation the volume extinction coefficient and radar reflectivity for a given type of hydrometeor and size ratio exhibit a power-law re-

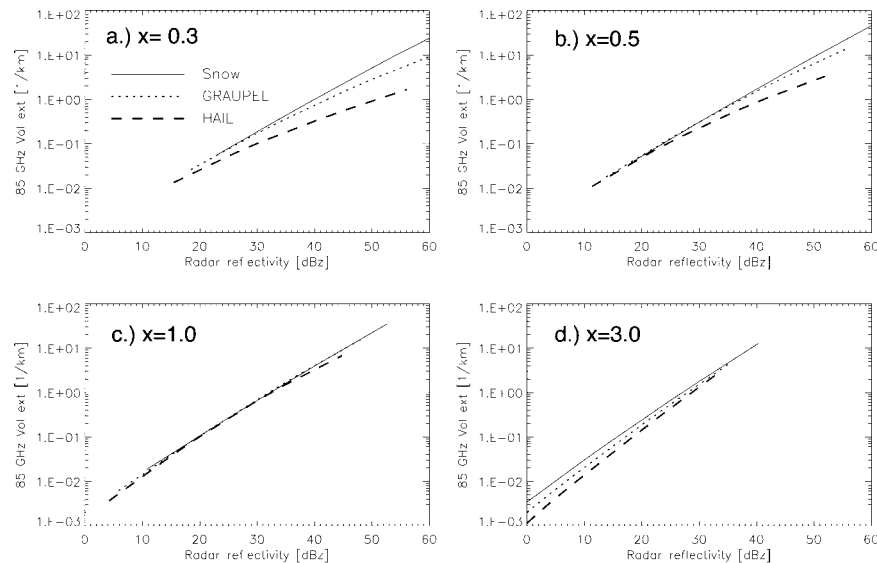


FIG. 3. Dependence of volume extinction coefficient on radar reflectivity for different size ratios x and different hydrometeor types.

lation. With increasing size ratio, the slope in the log-log plot increases, whereas the position of the curve moves from higher to lower radar reflectivities and from higher to lower volume extinction coefficients. Figure 3 shows the relation between volume extinction coefficient and radar reflectivity for the different hydrometeor types sorted by size ratio. Interestingly, for size ratios close to unity, all types of hydrometeors show almost the same dependence of the extinction coefficient on the radar reflectivity. We may therefore expect that within a large range of relative size ratios the actual density of the particles has less influence on their scattering properties than does their actual size, which should result in a less ambiguous assignment of microwave optical properties to given radar measurements. It does not, however, eliminate the ambiguity in the assignment of a precipitation intensity. For example, given a radar reflectivity of 40 dBZ, the volume extinction coefficient for all three types of frozen hydrometeors at $x = 1$ is 4.0 km^{-1} , and the associated precipitation intensity would be 8 mm h^{-1} for snow, 15 mm h^{-1} for graupel, and more than 20 mm h^{-1} for hail. Note that the more unambiguous relation between radar reflectivity and volume extinction results from partial compensation of different effects associated with the optical properties of the particles as well as with their fall speed characteristics. As the particles become larger (or denser), their number density decreases, but, at the same time, their scattering efficiency increases. Note that as long as the size parameter ($2\pi r/\lambda$) of the particles is smaller than roughly 10, the scattering and extinction efficiencies increase smoothly with size parameter ($2\pi r/\lambda$). A size parameter ($2\pi r/\lambda$) of 10 would for a frozen particle with density 0.1 g cm^{-3} at 85 GHz cor-

respond to a comparatively large liquid equivalent diameter of roughly 5 mm in diameter.

Figure 4 shows the single-scatter albedo and asymmetry factor for the different types of precipitation and for the different size ratios. For the particles with size ratio smaller or equal to unity the single-scatter albedo is always greater than 0.95, but the smaller particles show a significant decrease of the single-scatter albedo at low rain rates. This decrease is strongest for the least dense snow. The asymmetry factor is strongly affected by both the density and the size ratio. With decreasing density or increasing size ratio, the asymmetry factor increases, because larger particles exhibit a more intense forward scattering.

c. Frequency dependence of optical properties

Figure 5 intercompares the volume scattering coefficients for the four frequencies 19, 37, 85, and 150 GHz, which are representative of the window channels that are currently used for passive microwave remote sensing. In addition to the differences in the absolute value of the scattering coefficient, one can see that increasing the particle density in general yields a stronger dependence on the size ratio. Comparing 150 GHz with 85 GHz for snow, for example (Fig. 5, lower-left panel), there is very little difference between the different curves, whereas for hail the difference between the curves for $x = 0.3$ and $x = 3$ is roughly an order of magnitude. To a lesser extent this result is true also for 19 and 37 GHz. However, unless very intense and widespread precipitation is observed, these channels may not be well suited to retrieve scattering information because of their large footprint size and the dominance of the

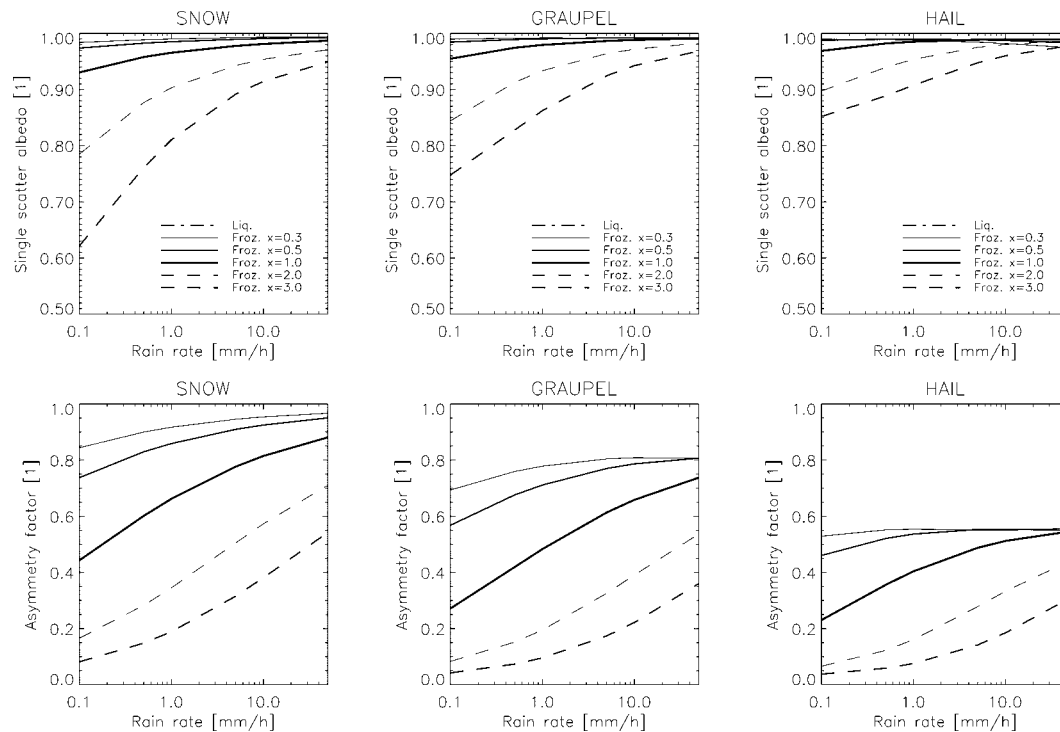


FIG. 4. Single-scatter albedo and asymmetry factor for the different precipitation types as a function of precipitation intensity.

emission signal of liquid precipitation and cloud liquid water. Despite the large differences in wavelength between the low- and high-frequency channels, the ambiguity introduced by variations in ice density seriously hampers the retrieval of information about the size of the ice particles from multichannel observations. A direct retrieval of ice particle size from the scattering intensities at different frequencies might only be possible if the particle density is known and is comparatively high.

The use of a channel at 150 GHz may, however, be of strong interest for precipitation retrieval over land surfaces, because the volume extinction of any given ice layer at 150 GHz is in most cases about a factor of 2–5 higher than that at 85 GHz. Thus, the observed response at 150 GHz may be larger than at 85 GHz, and precipitation detection may be facilitated. The effect of variations in cloud optical properties on the satellite-observed scattering index is quantified in the next section.

d. Passive microwave response to precipitation-sized ice

A number of remote sensing techniques for precipitation rely on detecting the depression observed in the passive microwave brightness temperatures when precipitation-sized ice particles are present. This depression results from a reduced bulk emissivity of the cloud top

when the constituent particles are strongly scattering. The net effect of scattering is to depolarize the signal at the same time as it depresses the overall brightness temperatures, a combination that allows scattering to be distinguished from cold but strongly polarized emission from the open ocean surface. The variable used in the current paper to quantify the apparent intensity of scattering is the scattering index S of Petty (1994a,b). It may be thought of as the brightness temperature depression relative to emission from a nonscattering atmosphere whose total transmittance yields the same degree of polarization. This definition of the scattering index allows one to isolate effectively the effects of scattering from those of other parameters to which the raw brightness temperatures are sensitive.

From the standpoint of radiative transfer modeling, the intensity of scattering is governed by the total amount of ice and its optical properties. For the particle size distributions and particle types used in this investigation, the optical properties of the ice layer are described by the three classical parameters: the extinction coefficient, single-scatter albedo, and asymmetry factor.

As a first step to theoretically quantifying the response of the scattering index to variations in passive microwave optical parameters, we set up a number of radiative transfer simulations using a highly simplified model with an ice layer of constant microphysical properties and an isotropic source of radiation from beneath. In this simple model, the scattering index is just the dif-

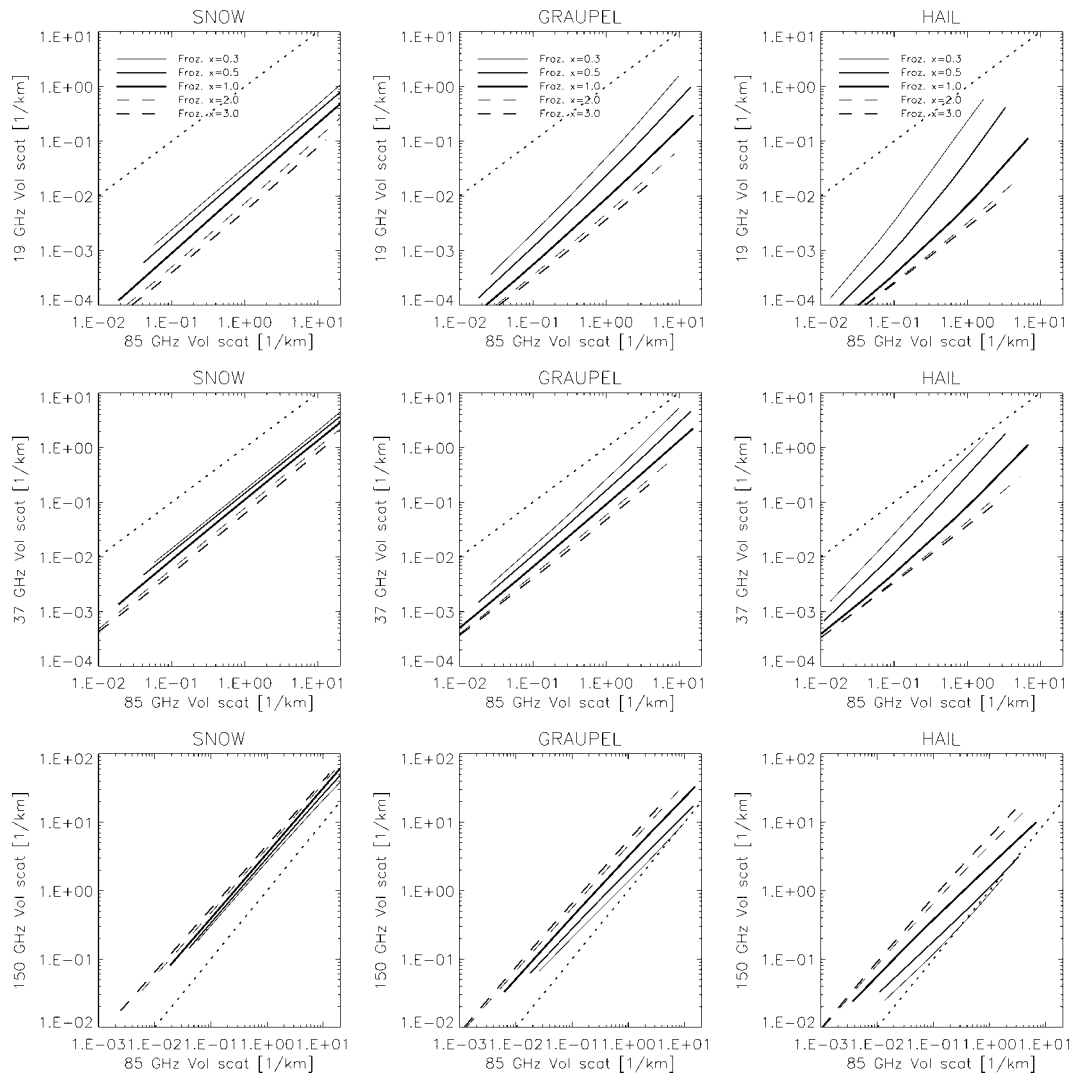


FIG. 5. Comparison of volume extinction coefficients for the different precipitation types. The abscissa always gives the 85-GHz volume scattering coefficient, and the ordinate gives (top) 19 GHz, (middle) 37 GHz, and (bottom) 150 GHz. The dotted line is the identity line.

ference between the isotropic upwelling radiation beneath the ice layer and the upwelling radiation above. The upwelling radiation above the ice layer consists of three parts: the transmitted radiation from below, the radiation that is emitted within the ice layer, and the downwelling radiation from above the ice layer, which is reflected toward the satellite. Within this simple model we do not consider variations in any parameters other than optical depth, single-scatter albedo, and asymmetry factor, nor do we consider any intercorrelations of cloud optical parameters (note that a more comprehensive treatment of radiative transfer is discussed in section 4, in which all relevant environmental parameters and intercorrelations are introduced and the model is compared with actual observations). Although the idealized results cannot reasonably be compared with actual ob-

servations, they provide insight into the relative effect of the different cloud optical properties on scattering index and thus enable an assessment of their relative importance for the understanding of the passive microwave response to frozen precipitation.

Figure 6 shows the results of the radiative transfer simulations. The four different sections show results for four different values of the single-scatter albedo, which was varied between 0.9 and 0.99. The asymmetry factor was varied between values of 0, representing isotropic scattering, and 0.9, which represents a strongly forward-scattering phase function. Optical depth was varied between 0.1 and 20. As can be seen from all four panels of Fig. 6, the effect of the asymmetry factor depends on the magnitude of the asymmetry factor itself. For a given single-scatter albedo and isotropic scattering with

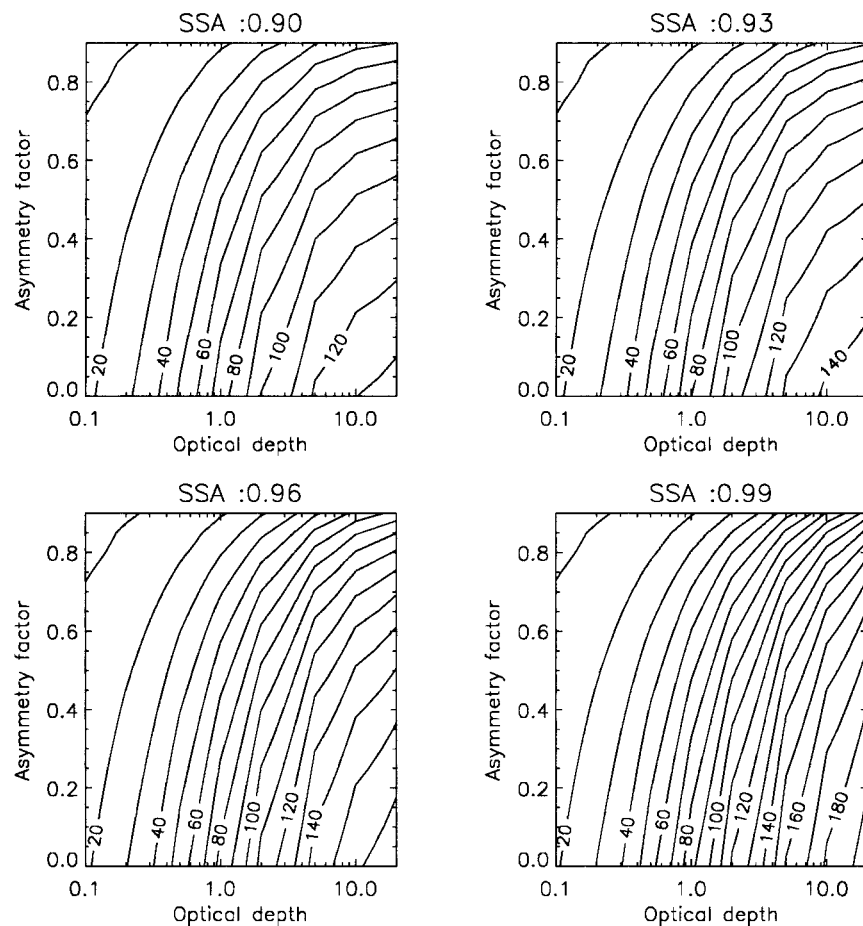


FIG. 6. Simulated scattering index as a function of the optical properties of the frozen precipitation. The isolines give the scattering index (K).

asymmetry factor close to zero, the variability of the scattering index is almost entirely governed by the optical depth. For high asymmetry factor, the scattering index becomes more dependent on the asymmetry factor itself, where an increase in asymmetry factor leads to a decrease in scattering index. This relationship is because with increasing asymmetry factor forward scattering becomes more pronounced and more warm radiation from below is scattered in an upward direction toward the satellite. In the limit of asymmetry factor equal to unity, only forward scattering would occur and, if the single-scatter albedo were unity, the upwelling radiation field at the satellite would be completely independent of the optical depth of the ice layer.

Variations in the single-scatter albedo do not affect this general functional relation. However, single-scatter albedo affects the magnitude of the observed scattering index. With decreasing single-scatter albedo, scattering becomes less pronounced and the emission of the ice layer becomes more dominant. In the limit of single-scatter albedo equal to zero the observed depression would be the difference between the emitting temper-

ature of the ice and the temperature of the upwelling radiation. This is the case for supercooled liquid water clouds with very little or no precipitation. From simple cloud liquid water absorption calculations, it can be shown that maximum scattering indices for nonprecipitating clouds do not exceed 10 K.

In the limit of single-scatter albedo equal to one, the ice layer does not emit any radiation at all and the observed scattering index is purely governed by the amount of back-scattered downwelling radiation from above the cloud and transmitted radiation from below the ice layer. The former contribution is generally small, because oxygen is a weak emitter and little water vapor is found above clouds with a significant amount of frozen precipitation. If there were no water vapor above the cloud, the downwelling radiation above the cloud would nearly equal the cosmic background radiation. Strong backscattering therefore leads to the lowest observed brightness temperatures and thus to the highest scattering indices. Thus, the highest values for the scattering index are found for single-scatter albedo close to

TABLE 2. Overview on overpass times and environmental conditions for the three cases of collocated SSM/I and radar data used in this study.

Case	I	II	III
Date (1995)	29 Aug	29 Sep	24 Aug
Time (UTC)	1930	0445	0915
Satellite	<i>F-10</i>	<i>F-13</i>	<i>F-10</i>
Precipitation type	Frontal	Moderate convection	Intensive convection
Radar echo top (km)	6–7	7	9–10
Columnar water vapor (SSM/I) (kg m^{-2})	27.5 prefrontal, 16.9 postfrontal	14.7	33.5

one (least emission) and asymmetry factor close to zero (least forward scattering).

4. Application

a. Dataset

In the course of this investigation we use combined radar and SSM/I observations observed during three different precipitation events in the period from August to September 1995 during the BALTEX–PIDCAP. During this experiment, radar volume scans of the SMHI-operated Gotland C-band radar were taken, timed according to overpasses of the *F-10* and *F-13* SSM/I. One radar volume scan consisted of 10 scans at different elevations, the lowest elevation being 0.5° and the highest being 15° , which were processed to pseudo-constant-altitude plan position indicator (CAPPI) layers with a vertical spacing of 1 km and a horizontal spacing of 2 km. The three precipitation events were observed under distinctly different meteorological conditions, thus producing different types of precipitation. Here, we describe the three cases used in this investigation (see also Table 2) and give a brief overview on the major synoptic situations that triggered the precipitation events.

1) CASE I

Case I is a frontal precipitation event from 29 September. The overpass time of the *F-10* was 1940–42 (UTC) and the radar volume scan started at 1930 and ended 1940. We selected this case because of the good coverage of both the SSM/I and the radar data, as well as because of the fact that it was the frontal event with the most intense precipitation observed during PIDCAP for which coincident radar and SSM/I data exist.

The upper panels of Fig. 7 show the observed SSM/I brightness temperatures at 85 GHz along with the pseudo-CAPPI radar reflectivity observed at 2 km altitude. One can identify a narrow band of high reflectivity approximately 1° east of Gotland. The frontal system was associated with a low pressure system with its center over Poland, which was slowly moving to the northeast. The location of the front itself was at that time very slowly moving eastward. In the SSM/I imagery one can identify some regions of scattering, most pronounced in

the southern part of the front, and a broad region of enhanced brightness temperatures near the coast of Poland. The water vapor fields derived from the SSM/I show a strong west–east gradient from about 17 kg m^{-2} in the western parts of the Baltic Sea to more than 30 kg m^{-2} in the eastern parts. Little or no liquid water is retrieved in the western parts, and more than 1 kg m^{-2} is retrieved near the Polish coast.

2) CASE II

Case II is a moderate convective event observed on 29 September, when the Baltic region was influenced by advection of exceptionally cold arctic air mass [on that day the Berliner Wetterkarte reported the coldest 850-hPa temperature measured in Berlin (-3.9°C) in September since 1950]. This synoptic situation was triggered by an extensive trough that had formed over western Europe and persisted over 5 days from 27 September to 3 October. As a consequence of this cold air advection, extensive convection cells were formed over the North Sea and the Baltic Sea as well as during daytime over Scandinavia and northern Germany and Poland. According to surface station reports, the convective cells were associated with intensive graupel and rain showers; accumulated rainfall rates for some precipitation stations exceeded 10 mm day^{-1} .

The convective cells can be identified clearly in the radar imagery and in the SSM/I brightness temperatures at 85 GHz (Fig. 7, middle panels). Apart from the lower spatial resolution of the SSM/I, the patchy structure of the radar data is seen even more strongly in the SSM/I data, where the superimposition of scattering and emission signals of precipitation cells in different development stages leads to cooler or warmer brightness temperatures, respectively, as compared with the precipitation-free background.

3) CASE III

The third case (see Fig. 7, lower panels and Table 2) is an intensive thunderstorm with its center north of Gotland. This convective event was part of a cluster of cells associated with a low pressure system that was moving northward from Germany toward Finland. The precipitation station at Visby (on Gotland), which is

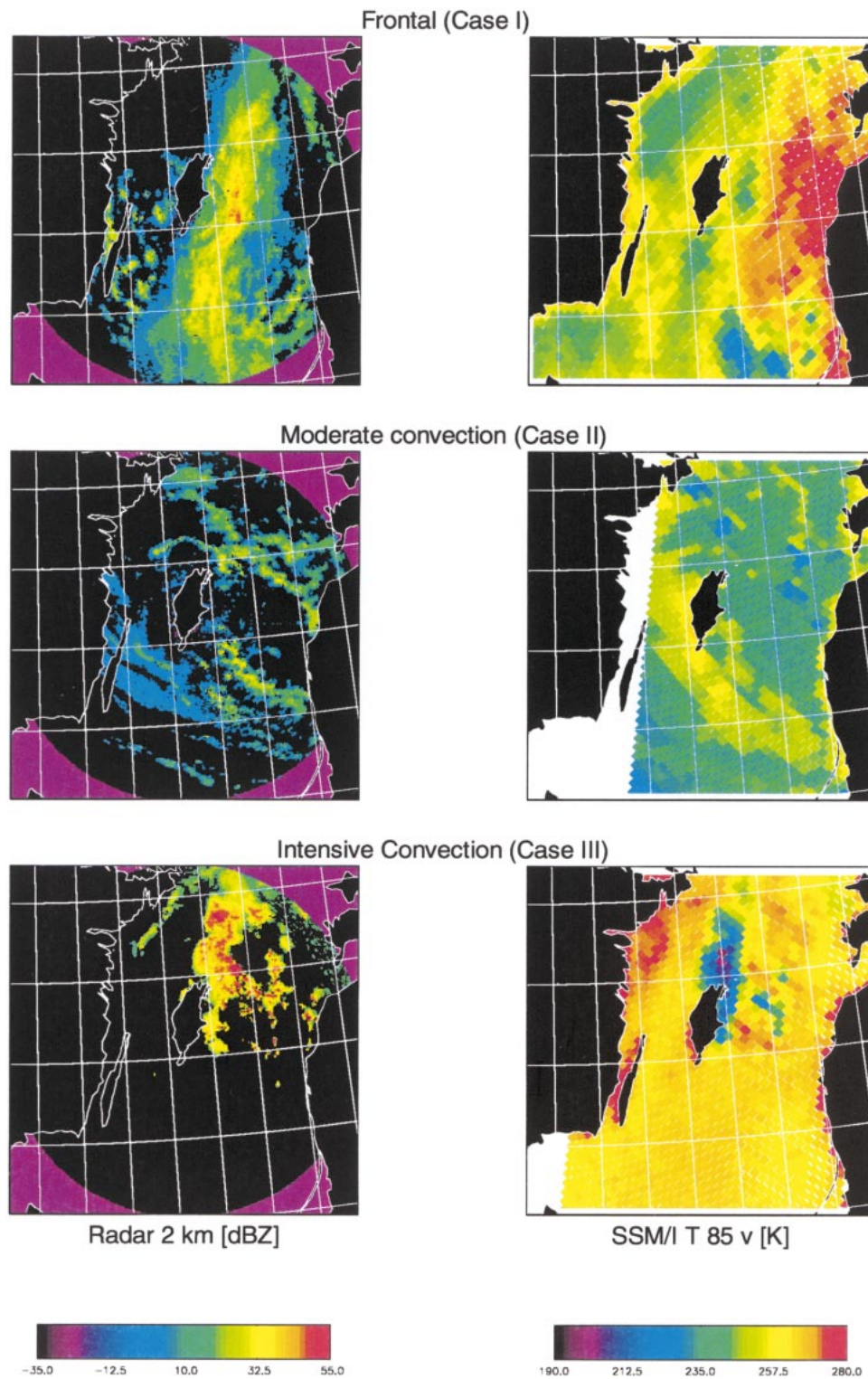


FIG. 7. Radar reflectivity and SSM/I brightness temperatures at 85 GHz, vertically polarized for the three precipitation systems investigated here. The radar data shown are pseudo-CAPPI for 2-km altitude.

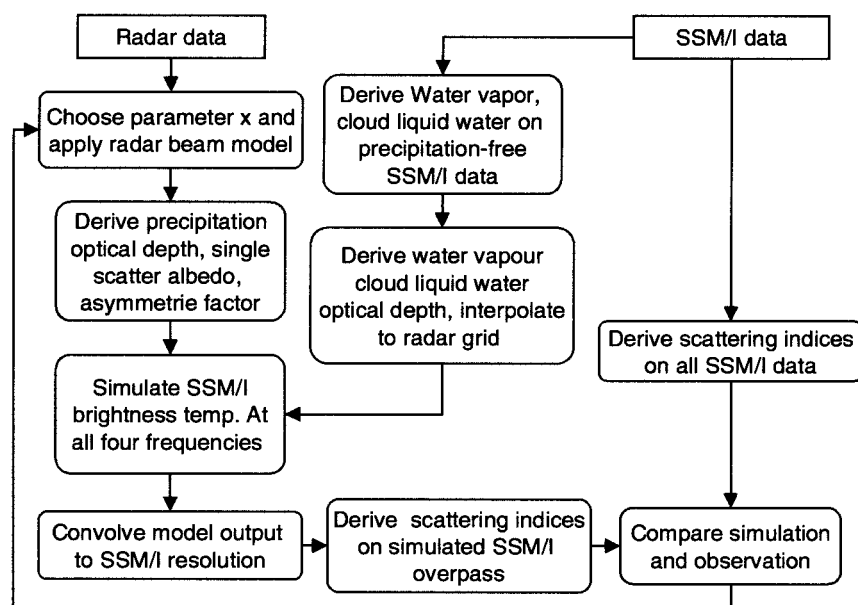


FIG. 8. Schematic view of the approach used to simulate passive microwave brightness temperatures and to intercompare scattering indices.

located at the southern edge of the thunderstorm, reported 12 mm of precipitation for 24 August in Stockholm; more toward the northwest, totals were only about 4 mm. Stations that were more directly affected by other cells of the cluster reported up to 30 mm of precipitation (Isemer 1996). The observed radar reflectivities exceeds 50 dBZ, and the maximum vertical extent of the convective system is about 10 km. The 85-GHz SSM/I brightness temperatures in the core of the convective cell reach minimum values below 200 K, where the background values in the precipitation-free regions are between 260 and 265 K.

b. Radiative transfer modeling

1) PREPARATION OF MODEL INPUT FIELDS

Figure 8 schematically depicts the approach we use to incorporate SSM/I and radar data into a common data evaluation scheme. From the SSM/I data we derived fields of water vapor content, cloud liquid water, and wind speed using the set of algorithms described in Petty (1994b). These fields are only used where possible rain contamination is small. For details of the rain-flagging and data interpolation, which are not of crucial importance in this context, we refer the reader to the original paper. To ensure further that the SSM/I data are free of land contamination, we rejected all measurements from the analysis that overlap land by more than 1%. For details of the derivation of this information and of the effect of mixed land–water pixels on SSM/I brightness temperatures and retrievals, see Bennartz (1999).

The resulting fields of SSM/I-derived cloud liquid water and water vapor were interpolated to the radar

grid, which exactly covers the area shown in Fig. 7, with a 2-km spacing (240×240 pixels) and were used as input for the liquid water and water vapor fields for the three-dimensional radiative transfer model. The cloud liquid water was taken to be uniformly distributed between the top of the precipitation layer (which we estimated from the radar data) and a cloud base that was fixed at 1-km altitude. The temperature profile was derived from surface temperatures assuming a standard lapse rate of 6.5 K km^{-1} . The water vapor was then vertically distributed so that relative humidities were at 85% outside the cloud and at 100% within the cloud. Note that the details of the vertical distribution of water vapor and cloud liquid water are of secondary importance for the model results, whereas the total column amount of water vapor and cloud liquid water and surface wind speed are of primary importance for the microwave brightness temperature in precipitation-free regions (Petty 1994b). The vertically resolved fields of water vapor and cloud liquid water were then converted to passive microwave optical properties using the Rosenkranz (1998) model for water vapor and the Petty (1994b) parameterization for cloud liquid water.

Optical properties of the precipitation were derived from the radar data using the above-outlined approach (section 2), in which we first chose a size ratio x and the type of frozen hydrometeor (i.e., its density and fall speed characteristics). Using this information we derived the complete size distribution properties for the radar volume. Passive microwave optical parameters (optical depth, asymmetry factor, and single-scatter albedo) were then derived using Mie theory at all four SSM/I frequencies. These three-dimensional fields of

optical depth, asymmetry factor, and single-scatter albedo were then combined with the optical depth obtained from the water vapor and cloud liquid water and were used to simulate high-resolution passive microwave images of the scene in question, using the backward Monte Carlo code of Petty (1994a). This radiative transfer code accommodates arbitrary three-dimensional rain cloud geometries. Although the model is not yet able to simulate fully polarized (vector) radiative transfer through the rain cloud itself, first-order polarization effects due to differential emission/reflection at the ocean surface are accounted for.

Because we are interested in the effect of variable ice particle size distribution and density, we varied these two parameters in different model runs. However, within each model simulation, size ratio and density were kept fixed at the predefined value.

The primary results of the radiative transfer simulations were brightness temperatures at the spatial resolution of the radar data. To allow for consistent intercomparisons with the SSM/I data, we convolved these simulated images to the resolution of the SSM/I at the four frequencies, thus simulating the SSM/I overpass in its native coordinates and resolution. A detailed description of the convolution technique can be found in Bennartz (1999).

This simulated SSM/I overpass was then subjected to the same analysis as was the actual SSM/I overpass. We applied the method of Petty (1994b) to derive scattering indices and compared the simulated and observed scattering indices. We performed model simulations for all four SSM/I channels; for all three hydrometeor types; and for size ratios of 0.2, 0.3, 0.5, 0.75, 1, 1.5, and 2; as well as for a control run without any hydrometeors.

The above-outlined approach overcomes several deficiencies of a conventional approach in which radar reflectivities are first convolved to rain rates using fixed $Z-R$ relations and then are compared with passive microwave scattering indices or rain rates. First, the radar and SSM/I data are interpreted with the same underlying physical assumptions. The passive microwave and radar optical properties are based on the same assumption about particle size distribution and fall speed. They further obey a simple but internally consistent precipitation model that makes use of all radar data in their native resolution.

2) INTERCOMPARISON OF SIMULATED AND OBSERVED BRIGHTNESS TEMPERATURES

Before evaluating the scattering signals, we compare the convolved simulated SSM/I brightness temperatures with the observed brightness temperatures. Note that because SSM/I data were used to derive some of the input fields such as liquid water path, column water vapor, and so on, the observed and simulated fields are not completely independent. Our primary interest, however, is, the scattering signal of ice particles, which, as

we subsequently show, is practically decoupled from the above information. The intercomparison of modeled and observed brightness temperatures is useful to assess the absolute performance of the model. Subsequently we show the results for Case I, which in this case is most interesting because of the strong gradients of columnar water vapor in a west-east direction caused by the differing prefrontal and postfrontal environments.

In Fig. 9, the results for 37 GHz and 85 GHz are shown by way of example (for a size ratio $x = 1$ and frozen hydrometeors assumed to be snow). The middle panels show the model results at 2-km horizontal resolution. Close to the radar site, artifacts of the pseudo-CAPPI layer boundaries can be identified. The spatial distribution of scattering areas at 85 GHz is well reproduced by the model. The strongly emitting regions west of the coast of Poland are in general well matched; however, the absolute brightness temperatures as well as the apparent variability of the SSM/I observations in this region are not reproduced by the model results.

Because of the larger footprint size at 37 GHz, the observed and convolved model data at this frequency are in general smoother. Again, the spatial structure of the observed data is well matched, but the absolute values might differ. Scatterplots of the modeled and observed brightness temperatures are shown in Fig. 10, and biases, rms errors, and correlations are listed in Table 3. Note that the high correlations that are obtained for all channels reflect the use of SSM/I-derived water vapor and cloud liquid water fields as input for the simulations and should not be interpreted in any physical way. However, they validate, to some extent, the processing of the simulated images. Model biases range from -12 K for 19 GHz, horizontally polarized, to $+6.4$ K for the polarization difference at 19 GHz. Note, that the low biases for 37V (vertical polarization) and 85V are caused by a partial compensation of positive and negative deviations of the model data, as seen in Fig. 10. In view of the large bias component in the rms error, the bias-corrected rms error yields a more realistic estimate of the relative accuracy of the model. These errors are about 4 K with a minimum of 2.84 K at 22 GHz for the vertically polarized channels and between 7 and 10 K for the horizontally polarized channels.

The deviations between the model results and the SSM/I observations presumably reflect the error contributions of several simplifications and assumptions used in the model. Likely candidates for the largest deviations are errors in estimation of the surface emission and of total column water vapor absorption, due to modest errors in the determination of wind speed and total water vapor amount and/or caused by biases in the parameterization of the resulting rough surface emissivity and water vapor mass absorption coefficient. Errors due to the scalar treatment of radiative transfer, the assumption of spherical precipitation particles, or systematic calibration uncertainties of the SSM/I itself, whose absolute calibration is accurate to 3K (Hollinger

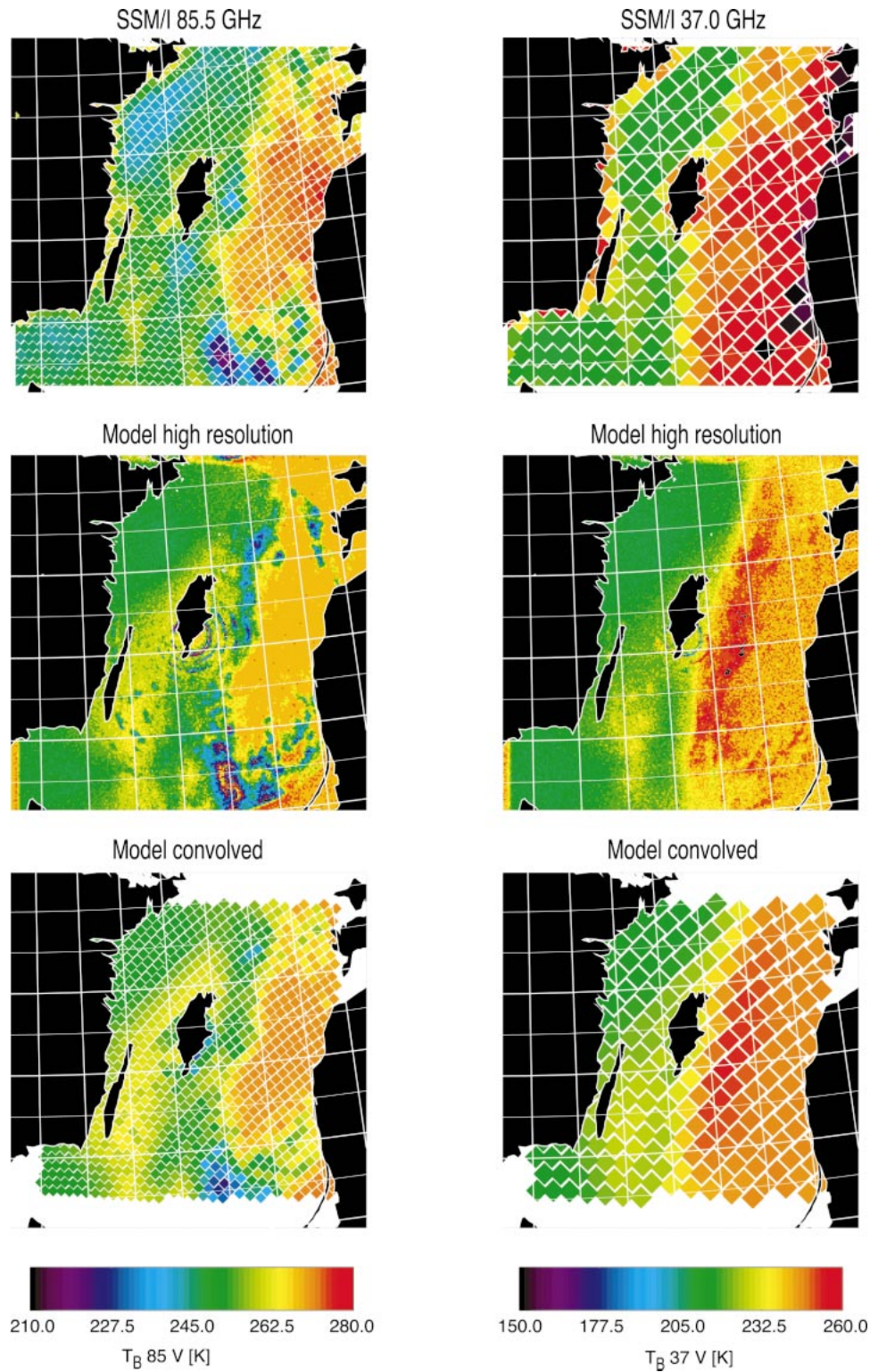


FIG. 9. Comparison of SSM/I observed and modeled brightness temperatures for (left) 85 and (right) 37 GHz, vertically polarized. The upper panels show the respective SSM/I observed brightness temperatures, the middle panels the results of the radiative transfer model at 2-km spacing, and the lower panels show the model results convolved to the respective SSM/I resolution.

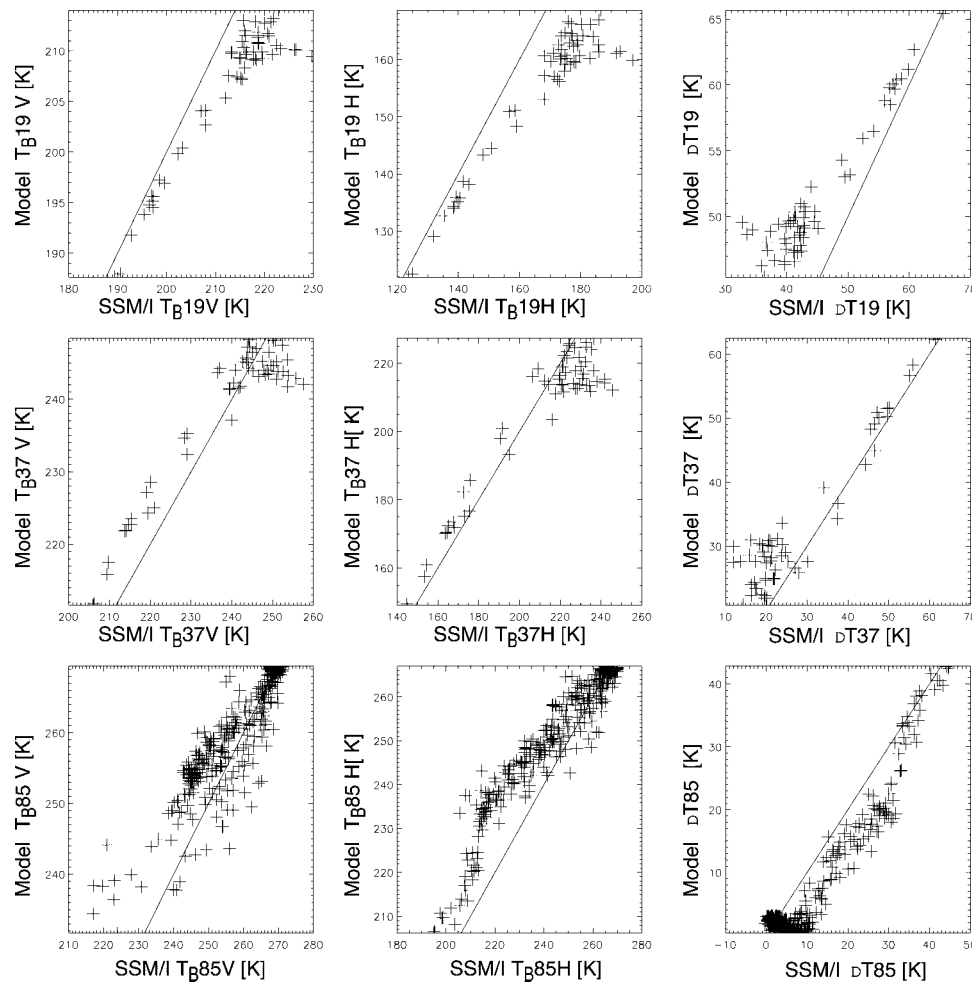


FIG. 10. Scatterplot of observed vs modeled (and convolved) brightness temperatures and polarization differences at (top) 19, (middle) 37, and (bottom) 85 GHz. Only data over homogeneous water surfaces are shown.

TABLE 3. Bias, rms error, bias-corrected rms error, and correlation of the modeled versus observed brightness temperatures and polarization differences. Scatterplots of the data are also shown in Fig. 10.

T_B	Bias (K)	Rmse (K)	Rmse (bias corrected) (K)	Correlation
19V	-5.62	6.92	4.05	0.946
19H	-11.98	14.09	7.41	0.950
19V - 19H	6.36	7.25	3.47	0.951
22V	-2.51	3.79	2.83	0.977
37V	0.68	6.15	6.00	0.941
37H	-3.65	11.56	10.59	0.944
37V - 37H	4.34	6.79	4.79	0.945
85V	-1.70	5.86	5.60	0.881
85H	-5.66	9.65	7.91	0.951
85V - 85H	-3.95	5.57	3.61	0.950

et al. 1987), are also possible but are less likely to produce large biases. The relatively small bias and the rms error at 22 GHz indicate that the water vapor absorption at this frequency at least is consistent with the strictly empirical algorithm used for the water vapor retrieval.

Regardless of the source of the biases in the background radiances, recall that the current investigation focuses on the effect of scattering by ice particles. By design, the scattering indices are insensitive to modest changes in the background fields and are governed primarily by the precipitation particles alone. That this case is indeed true will be seen in the results that follow.

c. Comparison of simulated and observed scattering index

We shall now compare the results of the different model simulations with respect to the sensitivity of the scattering index to particle size and density, with the observed SSM/I-based scattering index serving as the

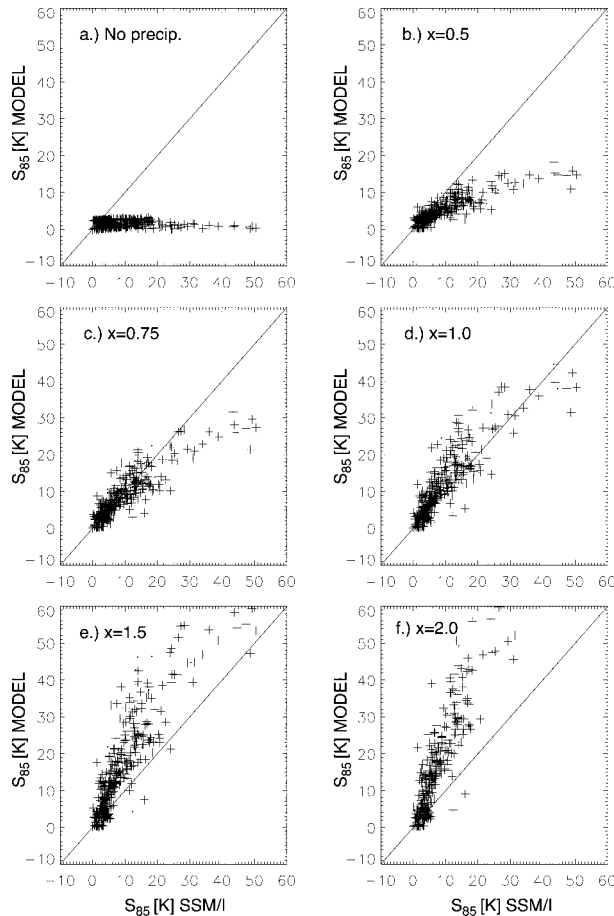


FIG. 11. Scatterplots of simulated vs observed scattering indices at 85 GHz for different values of the size ratio x for snow.

reference. For completeness, calculations were performed for hail, graupel, and snow for all three precipitation events, although the meteorological conditions for Case I were certainly not consistent with hail development. However, for Case I, the occurrence of both snow and graupel in different mixtures as well as different spatial distributions is likely. For Case II, the formation of graupel is most likely given that surface precipitation stations in the region observed graupel showers in this time period. The intensive-convection Case III is likely to allow for hail development.

A comparison between the observed and simulated scattering indices at SSM/I resolution is shown in Fig. 11 for snow. The obvious and expected result for the control run is that in the absence of precipitation no significant scattering is to be observed. With increasing size ratio (i.e., decreasing ice particle size), scattering becomes more intensive, and, at about a size ratio of $x = 1$, the observed and simulated scattering indices show the best agreement. For very large ice particles, the intensively scattering regions are systematically underestimated; for small particles, the scattering index is systematically overestimated. These results are in agree-

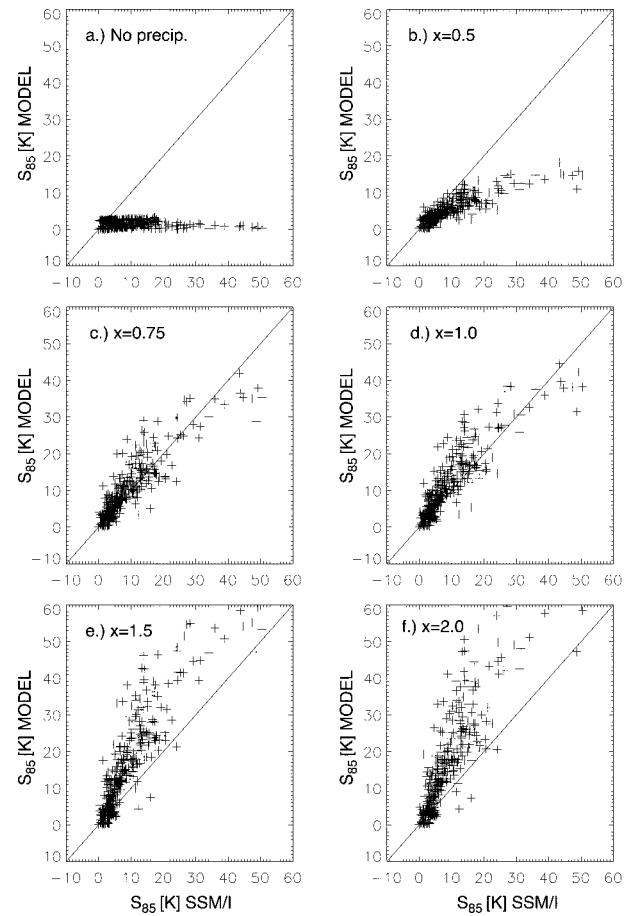


FIG. 12. Same as Fig. 11 but for graupel.

ment with section 3, where we showed that for a given radar intensity the extinction coefficients at 85 GHz decrease with increasing particle size (see Fig. 2 lower panels).

To show the effect of variable ice density we show the same results for graupel (Fig. 12). As shown in section 3, the optical properties for different hydrometeor types near $x = 1$ are almost identical. Therefore, little difference in the response of the scattering to the two different types of hydrometeors can be expected. Only for very small particles ($x = 0.5$) or very large particles ($x = 2$) might differences be expected. Note also from Fig. 3 that differences between the extinction coefficients at the different frequencies occur at low radar reflectivities for $x \gg 1$, whereas for $x \ll 1$ maximum differences occur at the high reflectivities. Because radar reflectivities in Case 1 are typically smaller than 30 dBZ (see, e.g., Fig. 8), we might further expect that differences in the scattering signature of snow and graupel in the simulation data only occur for high values of x . This is indeed the case: moderate deviations between Fig. 11 and Fig. 12 only occur for $x = 2$. This result once again highlights that particle density has less influence on the scattering signal than particle size does

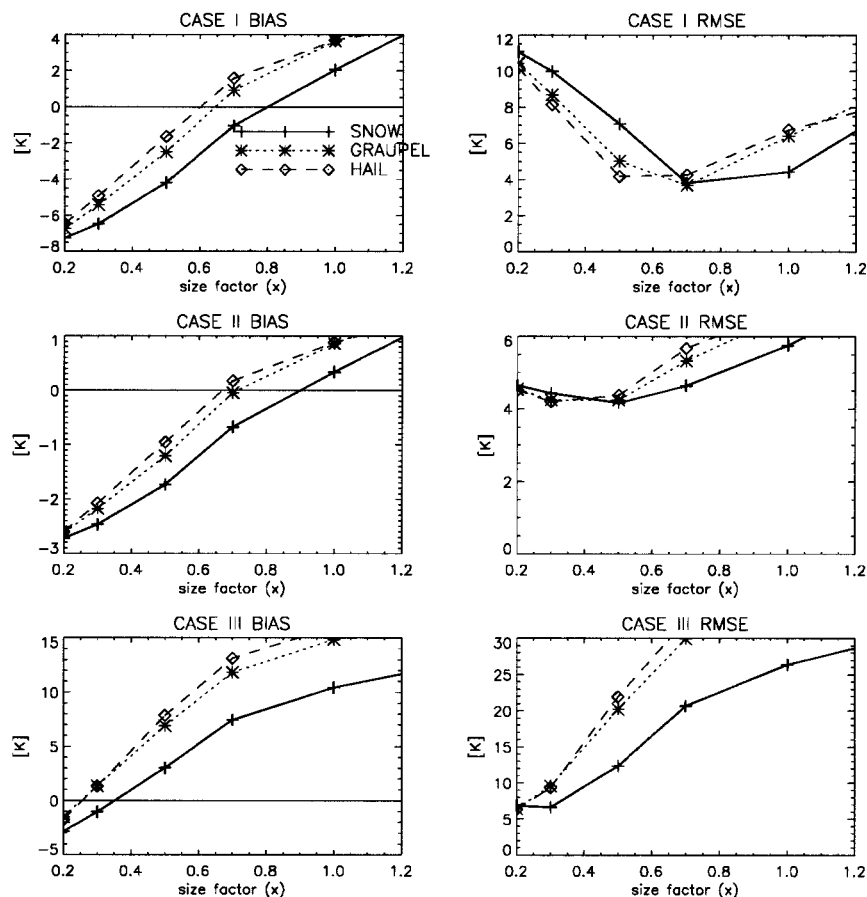


FIG. 13. Bias, rms error, and correlation between observed and simulated scattering indices as function of size ratio x for different types of precipitation.

and that these types of hydrometeors cannot be distinguished based on their scattering signature alone.

Figure 13 shows the rms deviation and bias between simulated and observed scattering indices as function of size ratio x and hydrometeor type for all simulations. For all three cases and hydrometeor types, the bias shows the same functional dependence on the size ratio x . For small x (i.e., large ice particles) the bias is negative, meaning that the scattering intensity is underestimated by the model. For high values of x the bias is positive, indicating an overestimation of scattering by the model. In general, the curves of graupel and hail are close to each other, and the bias of snow is in general lower. The differences between the biases of the three hydrometeor types are in general smaller than the absolute bias of the models as compared with the SSM/I-derived scattering indices. In most cases, the differences between the hydrometeor types do not exceed 2 K.

Despite this general behavior of all simulations, the size ratio for which the mean difference between the SSM/I-derived and the simulated scattering indices is zero differs significantly for the three cases. For Case I it lies between $x = 0.6$ and $x = 0.8$, depending on

density, but it varies between $x = 0.7$ and $x = 0.9$ for Case II and between $x = 0.25$ and $x = 0.35$ for Case III. The associated rms deviations between SSM/I-derived and simulated scattering indices are about 4 K (6 K for Case III) or about 10% of the overall variability of the scattering index. The values of x with zero bias are those where the physics of the simple model outlined in section 2 provides a solution that is consistent with both the radar and SSM/I observations. From these data it is thus possible to estimate the relative size of the frozen precipitation. We can therefore state that, in all cases, the effective melted diameters of the ice particles are somewhat larger than those for liquid precipitation, which is consistent with the findings discussed in other papers (e.g., Sekhon and Srivastava 1970). However, the size of the ice particles differs significantly for the three cases. In Case I, the ice particles are approximately 20% larger than liquid hydrometeors at the same rain rate, whereas in Case II they are only about 10% larger. Case III exhibits the largest ice particles, which are 4 times larger than the liquid hydrometeors.

At this point we have discriminated the particle size effect from the density effect on scattering index and

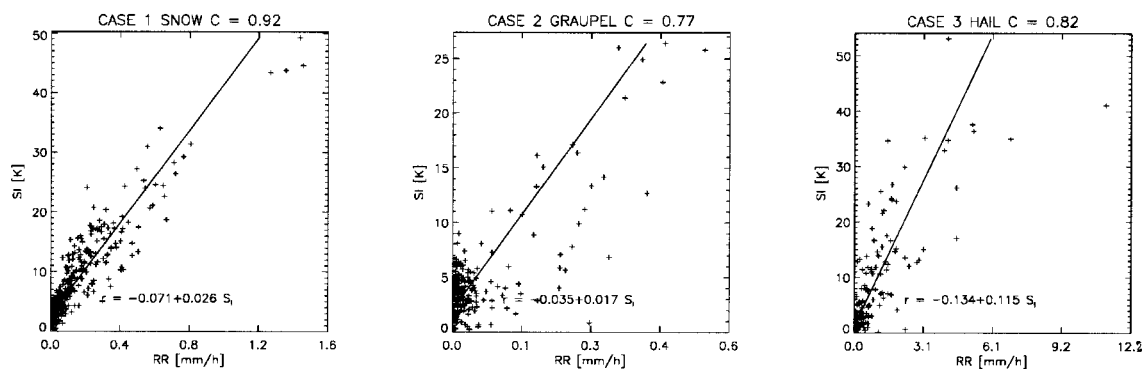


FIG. 14. Relation between radar-derived rain rate and SSM/I-derived scattering index at 85 GHz. The radar precipitation estimates were derived using the pseudo-CAPPI radar data at 4-km altitude. The radar-derived rain rates were convolved to the SSM/I's resolution at 85 GHz using the method described in Bennartz (1999), so that both radar and SSM/I data were mapped to the same grid and spatial resolution. The Z - R relation was chosen according to the particle sizes derived in section 4c.

have shown that ice particle density is of minor importance as far as the scattering signal itself is viewed. In the next section, we compare rain-rate estimates from the radar with the SSM/I-derived scattering indices and evaluate the effect of the above-discussed results on precipitation retrieval.

d. Effect on precipitation estimates

Observed variability in the relation between scattering index and radar-derived precipitation rate was the starting point of this paper. To highlight this issue further and to quantify its magnitude we show in Fig. 14 the results of a direct intercomparison of radar precipitation estimates and SSM/I-derived scattering indices for the three cases of precipitation events considered here. The Z - R conversion follows section 2. Because our main interest in this paper is the role of frozen precipitation in determining observed scattering at 85 GHz, we focus on pseudo-CAPPI radar precipitation estimates at 4-km altitude, thus ignoring processes within and below the melting layer.

The solid lines in Fig. 14 represent linear regressions between both datasets, whose parameters are shown in the lower part of the scatterplots. Correlation coefficients between 0.77 and 0.92 and linear relations between SSM/I-derived scattering index and radar-derived rain rate are obtained. Despite the high linear correlation of each single case, the regression highlights the difficulties that arise when using the scattering index as a fixed linear indicator for rain rate. Although Case I (frontal precipitation) shows a sensitivity of $16 \text{ K (mm h}^{-1})^{-1}$, Case II (cold-air outbreak, graupel shower) shows $58 \text{ K (mm h}^{-1})^{-1}$, and Case III (intensive convection) exhibits a sensitivity of $8.6 \text{ K (mm h}^{-1})^{-1}$. Correspondingly, a fixed scattering index of 30 K yields a rain rate of 1.9 mm h^{-1} for Case I, 0.5 mm h^{-1} for Case II, and 3.5 mm h^{-1} for Case III. Thus, despite the good linear relation for each single case, an apparent variability in the relation between scattering index and

rain rate of a factor of 6–7 is obtained for the different precipitation events. This variability is caused by the different particle sizes and densities of the different cases. As shown in section 4, the relation between scattering index and radar reflectivity is most strongly affected by variations in the particle size. If the radar reflectivity is converted to rain rate, the Z - R relation is affected by both the particle size and particle density (see Fig. 2, middle panels).

Thus, the choice of a suitable Z - R relation for the conversion of radar reflectivities to rain rate is of crucial importance when passive microwave precipitation estimates are compared with radar data. Furthermore, to derive instantaneous precipitation estimates from the scattering index, the relation between scattering index and derived rain rate cannot be kept fixed. When the sensitivities for the three cases investigated here are compared, our results indeed suggest that errors in the precipitation estimate within a factor of about 6 are likely to occur, if a fixed threshold is used for precipitation estimation.

5. Conclusions

Within the framework of this article we describe an approach that allows one to identify ice particle properties that are consistent with radar observations. We utilize this approach to investigate the effect of variations of particle size and density on the microwave scattering signature as observed by SSM/I. We find the following.

- 1) The relation between radar reflectivity and passive microwave optical parameters strongly depends on the particle size of frozen hydrometeors. The induced variability is almost entirely governed by the ice particle size and is only moderately affected by variations of ice particle density.
- 2) Although ice particle density is of minor importance for the relation between the scattering index and ra-

dar reflectivity, it has an effect on the conversion of radar reflectivities to precipitation rates. For given radar reflectivities, the precipitation rate will still vary by a factor of 2–3 dependent on particle type (snow, graupel, or hail).

- 3) The relation between rain rate and scattering index was found to be fairly linear for each of the precipitation systems investigated here, but the slope depends strongly on the type of precipitation. For intensive convection we found sensitivities of $9 \text{ K (mm h}^{-1})^{-1}$, but frontal precipitation exhibits sensitivities of $25 \text{ K (mm h}^{-1})^{-1}$, and small-scale graupel showers show sensitivities of more than $50 \text{ K (mm h}^{-1})^{-1}$.

In addition to physical processes that occur below the melting layer, it is likely that the relative size of the ice particles may vary depending on the type of precipitation. This variation partially explains the results obtained by Todd and Bailey (1995), who found systematic variations in the relation between rain rate and polarization-corrected temperature depending on the type of the precipitation.

With respect to global precipitation estimates from satellites, especially over land (where the scattering signal is the primary source of information concerning precipitation rate), the methods introduced here may serve as a first step toward identifying, understanding, and eliminating region- and storm-dependent biases. Based on the results shown here, it appears to be necessary to distinguish between different types of precipitation and to account for particle density and size variations between those types. Most important in this context is the need for considerable further research into the relationship between surface rain rate and microwave observables under various conditions. We believe that theoretical models and direct observations of radar reflectivities, satellite radiances, and cloud microphysical properties must continue to be used in a complementary fashion, because each has its own ambiguities and weaknesses.

The application of this approach might be especially useful in the framework of the Tropical Rainfall Measuring Mission, for which passive microwave data as well as spaceborne precipitation radar data are routinely available. Especially the availability of spaceborne radar data could significantly improve the usefulness of the methods outlined herein, given that no vertical beam-filling problems associated with the radar would occur. It would then be possible to derive more reliable in-

formation on the micro-physical properties of precipitating cloud over a variety of regions and under varying meteorological conditions.

Acknowledgments. The authors thank Daniel B. Michelson of SMHI for generously providing the radar data. Further, we thank Dr. Peter Bauer, who provided the Mie code used to derive the optical properties of the model. This work was made possible in part by a DAAD research fellowship to the first author. Additional support was provided by NASA Grants NAG8-1233 and NAG5-7741 (Tropical Rainfall Measuring Mission) to the second author.

REFERENCES

- Adler, R. F., A. J. Negri, P. R. Keehn, and I. M. Hakkarinen, 1993: Estimation of monthly rainfall over Japan and surrounding waters from a combination of low-orbit microwave and geosynchronous IR data. *J. Appl. Meteor.*, **32**, 335–356.
- Bauer, P., J. P. V. Poiares Baptista, and M. Delulis, 1999: The effect of the melting layer on the microwave emission of clouds over the ocean. *J. Atmos. Sci.*, **56**, 852–867.
- Bennartz, R., 1999: On the use of SSM/I measurements in coastal regions. *J. Atmos. Oceanic Technol.*, **16**, 417–431.
- Ferrier, B. S., 1994: A double-moment multiple-phase four-class bulk ice scheme. Part I: Description. *J. Atmos. Sci.*, **51**, 249–280.
- Grody, N. C., 1991: Classification of snow cover and precipitation using the Special Sensor Microwave/Imager. *J. Geophys. Res.*, **96**, 7423–7435.
- Hollinger, J., R. Lo, G. Poe, R. Savage, and J. Pierce, 1987: Special Sensor Microwave/Imager users guide. NRL Tech. Rep., Naval Research Laboratory, Washington, DC, 177 pp.
- Isemer, H. J., 1996: Weather patterns and selected precipitation records in the PID-CAP period, August to November 1995. GKSS-Rep. GKSS 96/E/55, 92 pp. [Available from GKSS Library, P.O. Box 1160, 21494 Geesthacht, Germany.]
- Kidd, C., 1998: On rainfall retrieval using polarization-corrected temperatures. *Int. J. Remote Sens.*, **19**, 981–996.
- Marshall, J. S., and W. Palmer, 1948: The distribution of raindrops with size. *J. Meteor.*, **5**, 165–166.
- Petty, G. W., 1994a: Physical retrievals of over-ocean rain rate from multichannel microwave imagery. Part 1: Theoretical characteristics of normalized polarization and scattering indices. *Meteor. Atmos. Phys.*, **54**, 79–100.
- , 1994b: Physical retrievals of over-ocean rain rate from multichannel microwave imagery. Part 2: Algorithm implementation. *Meteor. Atmos. Phys.*, **54**, 101–121.
- Rosenkranz, P. W., 1998: Water vapor microwave continuum absorption: A comparison of measurements and models. *Radio Sci.*, **33**, 919–928.
- Sekhon, R. S., and R. C. Srivastava, 1970: Snow size spectra and radar reflectivity. *J. Atmos. Sci.*, **27**, 299–307.
- Todd, M. C., and J. O. Bailey, 1995: Estimates of rainfall over the United Kingdom and surrounding seas from the SSM/I using the polarization-corrected temperature algorithm. *J. Appl. Meteor.*, **34**, 1254–1265.